Endogenic heat from Enceladus' south polar fractures: New observations, and models of conductive surface heating

Oleg Abramov *, John R. Spencer

Department of Space Studies, Southwest Research Institute, 1050 Walnut St., Suite 300, Boulder, CO 80302, USA

ARTICLE INFO

ABSTRACT

Linear features dubbed "tiger stripes" in the south polar region of Enceladus have anomalously high heat fluxes and are the apparent source of the observed plume. Several explanations for the observed activity have been proposed, including venting from a subsurface reservoir of liquid water, sublimation of surface ice, dissociation of clathrates, and shear heating. Thermal modeling presented in this work, coupled with observations from the Cassini Composite Infrared Spectrometer (CIRS) instrument, seeks to elucidate the underlying physical mechanism by constraining vent temperatures and thermal emission sources, using a model in which the observed thermal signature results primarily from conductive heating of the surface by warm subsurface fractures. The fractures feed surface vents, which may themselves contribute to the observed thermal emission. Model variables include vent temperature, presence of a surface insulating layer, vent width, time-variable heat input, and heat sources other than the central vent. Results indicate that CIRS spectra are best fitted with a model in which the surface is heated by narrow vents at temperatures as high as 223 K. Although equally good fits can be obtained for vent temperatures in the range of 130 to 155 K if the vents are wider (180 m and 22 m respectively) and dominate the emission spectrum, these models are probably less realistic because vents with these temperatures and widths cannot supply the observed H_2O vapor flux. The lack of emission angle dependence of the thermal emission when July 2005 and November 2006 CIRS observations are compared also argues against thermal emission being dominated by the vents themselves. Thus, results favor high-temperature models, possibly venting from a subsurface liquid water reservoir. However, a fracture filled with liquid water near the surface would produce significantly higher radiances than were detected unless masked by a thermally insulating surface layer. Models that best match the CIRS data are characterized by small fractions of the surface at high temperatures, which strengthens the case for the vents and/or their conductively-heated margins being the primary heat source. Models where the thermal emission is dominated by conductive heating of the surface from below by a laterally-extensive buried heat source cannot reproduce the observed spectrum. Models with a 10 cm thick upper insulating layer produce a poor match to the CIRS spectra, suggesting high thermal inertias near the tiger stripes. Finally, tiger stripe thermal emission measured by CIRS varied by less than 15% over the 16 month period from July 2005 to November 2006.

1. Introduction

The south polar region of Enceladus, a small icy satellite of Saturn, consists of young, tectonically deformed terrain dominated by roughly parallel, 2-km wide linear depressions dubbed "tiger stripes" (e.g., Porco et al., 2006). Recent observations by multiple instruments on the Cassini spacecraft describe an anomalously high heat flux associated with these tiger stripes, along with active plumes of water vapor and ice particles that originate from them (Porco et al., 2006; Spencer et al., 2006; Hansen et al., 2006; Waite et al., 2006; Spahn et al., 2006; Spitale and Porco, 2007).

Several explanations for the observed elevated temperatures and the resulting plume have been proposed, including venting from a subsurface reservoir of liquid water (Porco et al., 2006; Schmidt et al., 2008), sublimation of surface ice (Spencer et al., 2006), decompression and dissociation of clathrates (Kieffer et al., 2006), and shear heating (Nimmo et al., 2007). These mechanisms predict a range of vent temperatures: ~140 K for clathrate decompression (Kieffer et al., 2006), >180 K for sublimation of H_2O (Spencer et al., 2006), and up to 273 K for the shallow reservoir of liquid water (Porco et al., 2006). The elevated vent temperatures would conductively heat the nearby surface, contributing to the thermal signature observed by Cassini. The thermal modeling presented in this work, coupled with observations from the Cassini CIRS instrument, seeks to constrain the vent temperatures

* Corresponding author. Fax: +1 303 492 2606.
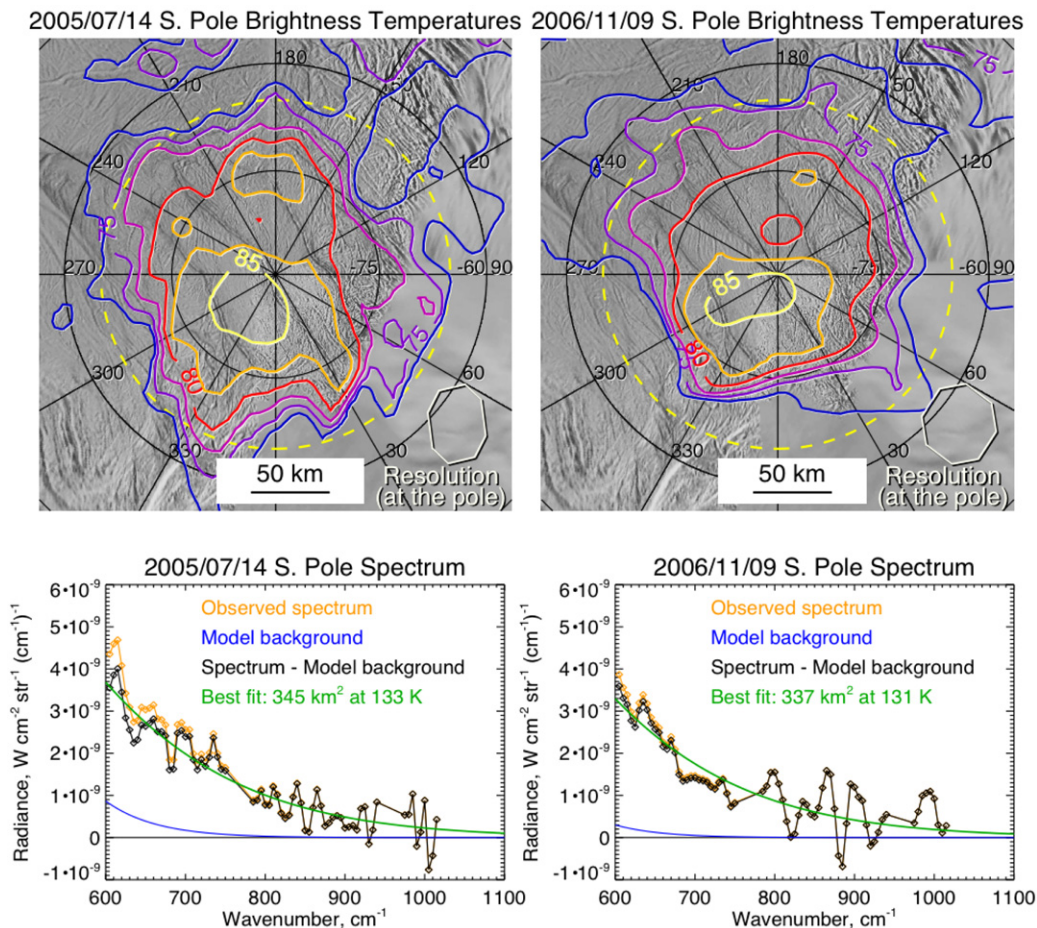 *E-mail address:* oleg.abramov@Colorado.edu (O. Abramov).

Fig. 1. Top: Maps of the Enceladus south polar 9–16 μm brightness temperature distribution from the July 2005 and November 2006 flybys. For July 2005 flyby, the subsolar latitude is 23° S, the subspacecraft latitude is 46° S, south polar emission angle is 44°, range to Enceladus is ~80,000 km, and spatial resolution is 23 × 32 km. For November 2006 flyby, the subsolar latitude is 16° S, the south polar emission angle is 22°, the subspacecraft latitude is 68° S, range to Enceladus is ~110,000 km, and spatial resolution is 32 × 35 km. The temperature distribution is probably consistent, within the noise, between the two maps, though overall temperatures are somewhat lower in 2006 due to cooling of the passive (solar-heated) background as southern winter approaches. Bottom: Average spectrum south of 65° S (yellow dashed line on the maps) for the two flybys, before and after correction for emission from a model passive background (blue line). The best-fit graybody curve to the two background-corrected spectra (green line) is very similar, indicating little dependence of thermal emission on emission angle.

and thermal emission source, and thus potentially elucidate the underlying physical mechanism.

2. Summary of observations

Observations of Enceladus' south polar thermal emission were conducted using Cassini's Composite Infrared Spectrometer (CIRS) (Flasar et al., 2004) instrument. Although optimized for atmospheric spectroscopy, CIRS is also used to investigate thermal radiation from the surfaces of icy satellites to constrain physical properties and detect possible endogenic activity. CIRS consists of two Fourier transform spectrometers, one using a 16–1000 micron detector with low spatial resolution (4 mrad field of view), and the other using two 1 × 10 arrays of 7–9 and 9–16 micron detectors with much higher spatial resolution (0.3 mrad field of view). Most of the endogenic heat measurements have been made using the 9–16 micron detectors.

2.1. July 2005 flyby

On July 14, 2005, the Cassini spacecraft flew by Enceladus with a closest approach of 168 km at a subspacecraft point of 24° S 326° N, and an approach trajectory that provided an excellent view of the south polar region. CIRS global mapping at 25 km resolution resulted in the discovery of a large region of elevated temperatures near the south pole (Spencer et al., 2006, and Fig. 1), which

correlates closely with the location of the tiger stripes. Scattered "ridealong" CIRS observations at 0.6–20 km resolution confirmed localization of warm material along the tiger stripes. The most powerful spectrum obtained corresponds to a maximum temperature of 145 ± 14 K in a two-temperature fit, and the average south polar spectrum south of 65° S can be fit with a blackbody at 133 ± 12 K occupying ~345 km². The total non-solar radiated power for the south polar region is estimated as 5.8 ± 1.9 GW.

2.2. November 2006 flyby

This more distant flyby, on November 8–9, 2006, provided views of the south pole from a minimum range of 90,000 km. CIRS obtained a map of the south polar region from 00:09 to 00:54 UT on November 9th from an average sub-spacecraft direction of 239 W, 68 S, giving an emission angle of 22° at the south pole, compared to 44° for the July 2005 flyby, where the sub-spacecraft point was at 176 W, 45 S. The view direction was just 14° from the orientation of the tiger stripes (which averages ~225 W), compared to 49 degrees in July 2005. Both these geometric factors allowed a more direct view into the interior of the tiger stripe fractures in November 2006 than in July 2005. However, the two data sets yielded very similar spectra and temperature estimates (Fig. 1). After subtraction of the passive background, the average south polar spectrum south of 65°
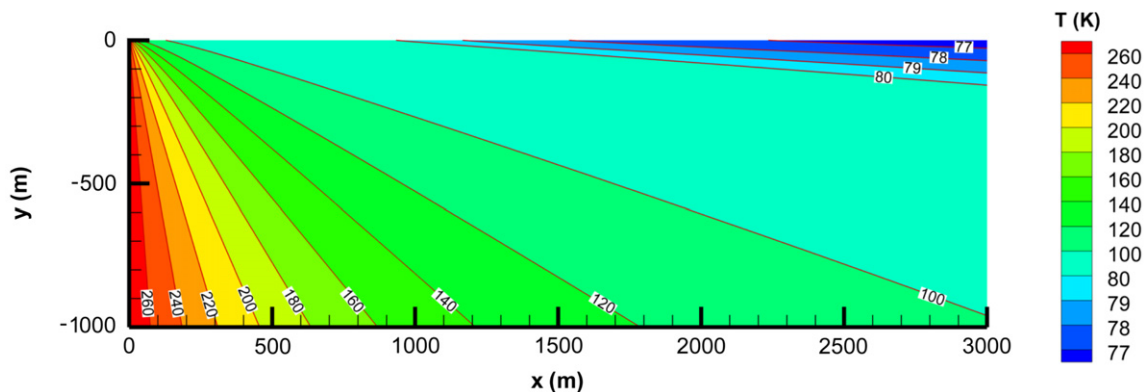
Fig. 2. Schematic of the thermal model, showing temperature vs depth (y) and distance from the warm fracture (x) for a fracture temperature of 273 K, the highest tested. The surface temperature distribution (at $y = 0$ m), including the contribution from the identical temperature distribution on the other side of the fracture, is used to generate a model CIRS spectrum, which is then compared to the Enceladus CIRS data. This plot shows only the surface that would be sampled by a CIRS footprint centered on the fracture—the full model dimensions are 40 km in the horizontal and 10 km in the vertical.

S is best fit by a graybody spectrum with a 650 cm^{-1} radiance of $2.72 \pm 0.21 \times 10^{-9}$ W cm^{-2} str^{-1} (cm^{-1})$^{-1}$ in July 2005 and $2.41 \pm 0.21 \times 10^{-9}$ W cm^{-2} str^{-1} (cm^{-1})$^{-1}$ in October 2006—a statistically insignificant change. This suggests that the thermal emission is dominated not by the fissures themselves, which would probably show higher temperatures at smaller emission angles as emission from deeper into the fissures can reach the spacecraft, but by the surrounding conductively heated surface. The total nonsolar radiated power for the south polar region is estimated as $5.4^{-1.5}_{+2.8}$ GW, which is comparable to the 5.8 ± 1.9 GW estimate from the July 2005 flyby (errors in radiated power are dominated by uncertainties in the best-fit temperature, not uncertainties in the measured flux). Thus, no significant change in total power output was seen in 18 months, suggesting a relatively steady-state process on this timescale.

3. Modeling technique

Temperature distributions around tiger stripes on Enceladus were modeled in two dimensions using HEATING 7.3, a multidimensional, finite-difference heat conduction code developed at Oak Ridge National Laboratory (Childs, 1993). The basic setup of the model is illustrated in Fig. 2. Our two-dimensional model includes heat transfer by conduction in the subsurface from a vertical fracture held at constant temperature, and by radiation at the surface. The HEATING materials library provides temperature-dependent thermophysical parameters appropriate for pure water ice over the full range of temperatures in the model. Emissivity of fresh water ice ranges from ∼0.94 to over 0.99 at the wavelengths of interest (e.g., Wan et al., 1994), and is set to 1 for the purposes of this model. However, other emissivity values were also tested, and it was found that the difference in temperature distributions produced at emissivities of 0.9 and 1.0 is only ∼1–2 K.

For all models, the bottom and right boundaries are insulating, and heat is lost by radiation through the upper boundary, which is radiatively heated to an equilibrium temperature of 75 K, close to the overall south polar temperature of 69 K expected in July 2005 for a surface with albedo of 0.8 (Spencer et al., 2006) and emissivity of 1. The left boundary represents the wall of the fracture, and is heated to a constant temperature in steady-state models. The geothermal gradient in the south polar region of Enceladus is not well known, and is therefore not included in the models. However, the lack of a geothermal gradient does not influence the surface temperature distribution, and thus affect the results, in any significant way (F. Nimmo, personal communication).

The model dimensions are 40 km in the horizontal and 10 km in the vertical. The right boundary is sufficiently far away from

the fracture to avoid boundary effects, essentially creating an infinite half-space. The horizontal resolution is 10 cm between 0 and 40 m, 10 m between 40 m and 4 km, and 50 m between 4 and 40 km. The vertical resolution is 10 cm between 0 and 20 m below the surface, 10 m between 20 m and 1 km, and 50 m between 1 and 10 km. This allows very fine-scale, 10-cm resolution in the area of interest at the surface and near the fracture. The model with a 10-cm insulating upper layer (Section 4.2) has an even finer resolution of 1 cm within the insulating layer. These resolutions were chosen by trial-and-error: the resolution was increased until the resulting surface temperature distribution in the steady-state model no longer changed.

Both steady-state and transient models have been developed. In the steady state model, the left boundary is held constant at a range of temperatures to model the heating of the fracture walls by plume gases (Nimmo et al., 2007) or liquid water (Porco et al., 2006). The resulting temperature distribution is then fed to a transient model to determine the thermal evolution of the area after the heating is shut off. Diurnal temperature variations are not included in the transient model because they are relatively minor in the polar region, especially near the tiger stripes, where the thermal conductivity is likely high (Section 4.2).

After the models are run for a range of temperatures, the resulting surface temperature distributions (on both sides of the fracture) are used to calculate 9 to 16 μm (600 to 1100 cm^{-1}) emission spectra at the resolution of the CIRS observation of interest, with the footprint centered on the fracture. In the simplest models, thermal emission from the fracture itself is ignored, based on the apparent lack of emission angle dependence of the south polar spectrum discussed above. The model spectra are then compared to the CIRS spectrum using an algorithm that calculates the mean square residual between the two spectra. In slightly more sophisticated models, the width of the fracture is also varied to produce the best possible fit to the CIRS spectrum for any given fracture temperature.

4. Results

4.1. Baseline model

The baseline model is based on varying a single parameter—the vent temperature—to produce a steady-state surface temperature distribution that fits a CIRS spectrum. To accomplish this, a range of vent temperatures from 175 to 273 K was tested. An example of a steady-state temperature distribution near an active vent on Enceladus is shown in Fig. 3 for a vent temperature of 273 K, the highest investigated. Fig. 4 shows a comparison of thermal emis-
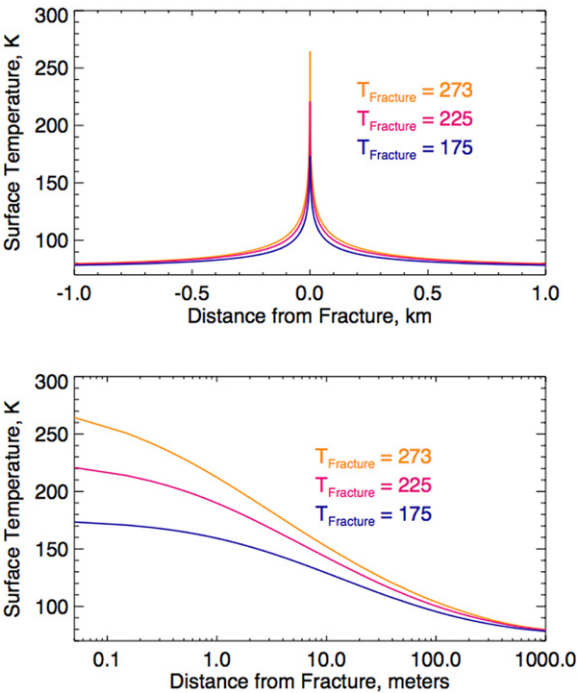
Fig. 3. Steady-state thermal model of the vicinity of a vent on Enceladus. Thermal and physical parameters of pure ice are assumed, and vent temperature is held constant. Temperature distribution is very sharply peaked with a scale length of ~10 m.

Table 1
Mean square residuals (MSRs) for comparisons between CIRS spectra from regions 5 and 6 (Fig. 4), and model spectra 1.

Region 5		Region 6	
Model fracture temperature	MSR	Model fracture temperature	MSR
210 K	5.57	180 K	4.30
215 K	5.39	185 K	4.13
220 K	5.00	190 K	4.06
221 K	5.05	191 K	4.05
222 K	4.99	192 K	4.04
223 K	4.97[a]	193 K	4.04
224 K	5.03	194 K	4.04
225 K	5.01	195 K	4.00[a]
226 K	5.04	196 K	4.14
227 K	5.06	197 K	4.12
228 K	5.07	198 K	4.17
229 K	5.11	199 K	4.18
230 K	5.12	200 K	4.15
235 K	5.45	205 K	4.39
240 K	5.95	210 K	4.84

MSRs are in units of radiance squared $(W \, cm^{-2} \, str^{-1} \, (cm^{-1})^{-1})^2$. Fracture width is zero meters.
[a] Lowest MSRs (best fits).

parison to the models because they show the strongest signal and are close to Cairo Sulcus.

The model was fit to the spectra by running the model at fracture temperature increments of 1 K and comparing the model spectra to CIRS spectra with a routine that calculates the mean square residual between the two curves (Table 1). The best fits to the CIRS spectra were obtained at a fracture temperature of 223 K for region 5 and 195 K for region 6 (Figs. 5a and 5b).

Despite its simplicity and its single free parameter, the model matches both the shape (described to first order by a single parameter, the color temperature) and absolute flux of these spectra: our ability to fit two data parameters with a single model parameter makes it at least plausible that this model approximates reality. Note that no large fissure is apparent in region 6, despite the good model fit: perhaps a smaller active fissure is present in this region.

The collimation of the observed plumes suggests that they issue from the warm fractures themselves rather than their
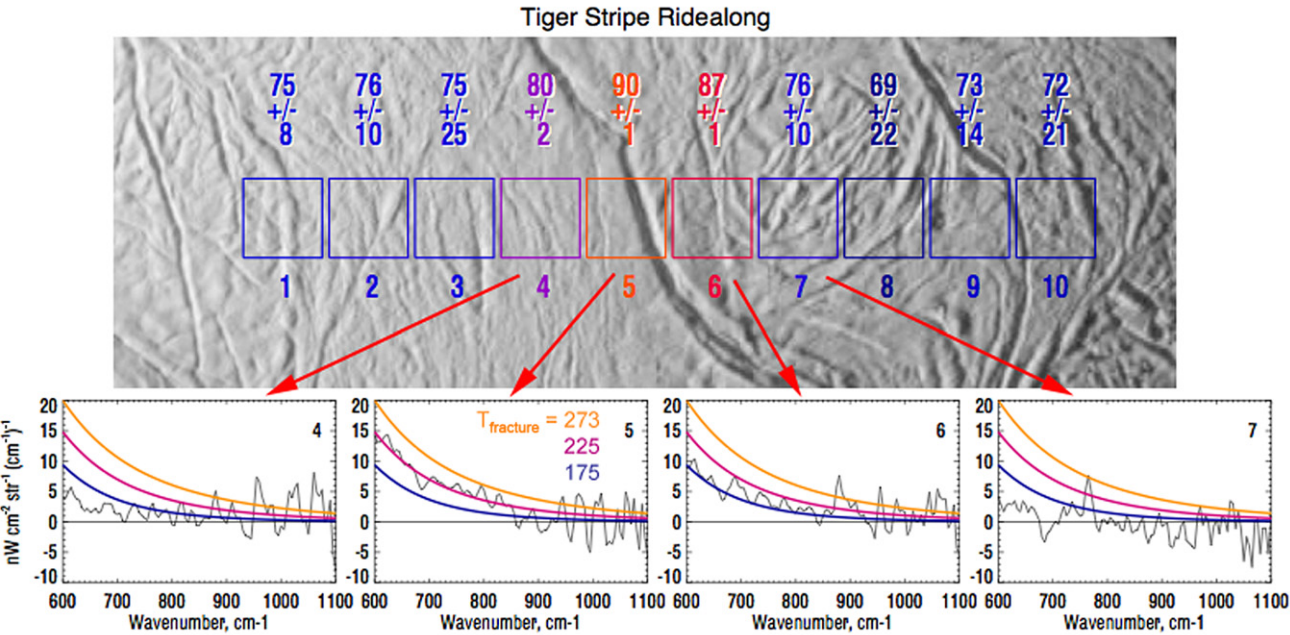
sion curves derived from surface temperatures produced by the model and the Cassini CIRS spectra acquired in the south polar region in the vicinity of the tiger stripe Cairo Sulcus, centered on hot source "B" of Spencer et al. (2006) at 84° S, 137° W. These data provide the highest spatial resolution (6 km/pixel) view of thermal emission from a tiger stripe, with good pointing knowledge thanks to simultaneous imaging, obtained during the July 2005 flyby. We have chosen spectra from regions 5 and 6 in this dataset for com-

Fig. 4. (Top) Each box shows the field of view of a single detector of the CIRS 9–16 micron array and its associated brightness temperature, with uncertainties. Field of view size is 6.0 km. (Bottom) CIRS spectra obtained from each indicated region, with superimposed model fits for fracture temperatures of 273, 225, and 175 K. Note that the model assumes the warm fracture is in the center of each CIRS field of view.
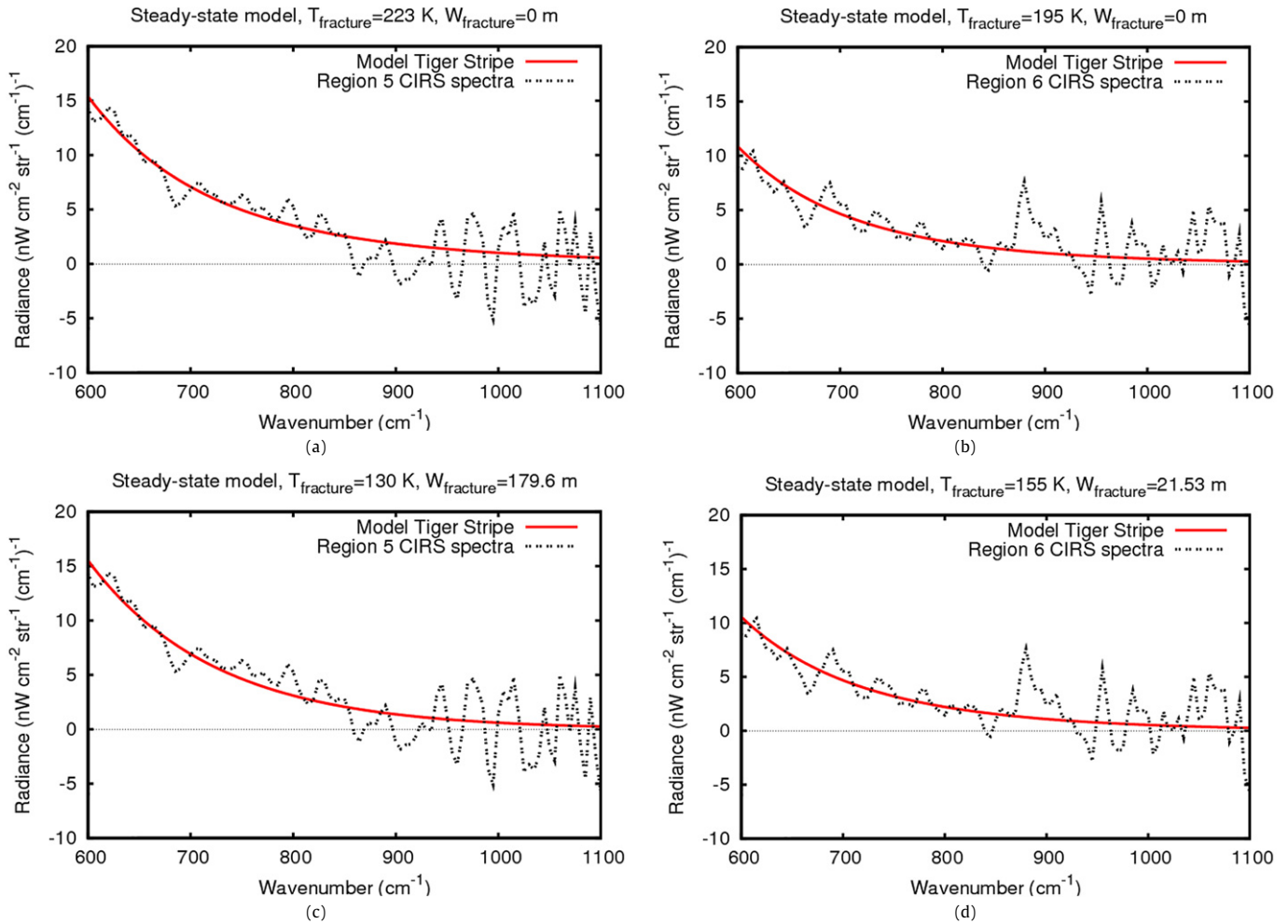
Fig. 5. (a) Best model fit to the region 5 CIRS spectrum with a fracture width of 0 m. Best-fit fracture temperature is 223 K. (b) Best model fit to the region 6 CIRS spectrum with a fracture width of 0 m. Best-fit fracture temperature is 195 K. (c) Best model fit to the region 5 CIRS spectrum with a variable fracture width. Best-fit fracture temperature is 130 K at the fracture width of 180 m. (d) Best model fit to the region 6 CIRS spectrum with a variable fracture width. Best-fit fracture temperature is 155 K at the fracture width of 22 m.

conductively-heated margins. From the vapor pressure of ice (Bryson et al., 1974), four 130 km long fractures (consistent with the observed tiger stripe geometry, (Porco et al., 2006)) at 225 K require a mean width of just 8 cm to supply the 150 kg s^{-1} of H_2O vapor inferred from stellar occultations (Tian et al., 2007) if the vapor escapes at thermal speeds. Bulk motion of the plume gases will reduce the necessary width further still. The thermal emission from an 8 cm wide fracture is negligible compared to that from its conductively-heated margins, consistent with our neglect of fracture thermal emission in our simple model.

Sublimation from the fracture margins must also be considered. From our model temperature distributions, assuming a water ice surface, sublimation along the margins of four 130 km long 225 K fractures produces water vapor at a rate of 500 kg s^{-1}. This is several times the observed plume production rate: perhaps the sublimation of the margins is inhibited by formation of a non-volatile lag deposit. Virtually all the marginal sublimation comes from within 1 meter of the fracture, and the lag deposit of this size would be too narrow to be detectable with current data.

Total heat flow from this model, assuming four 130 km long fractures, is 3.3 GW for 225 K fractures and 3.9 GW for 273 K fractures. These numbers are at or just below the 1-sigma lower limit of the observed total heat flow (5.8 ± 1.9 GW, Spencer et al., 2006). If our model is correct and most of the heat is indeed carried to the surface by conduction at temperatures below the melting point of water, the discrepancy might be explained if the

tiger stripes contain multiple active parallel fractures along some portion of their lengths, increasing total fracture length and thus total heat flow.

4.2. Effects of an insulating upper layer

Cassini CIRS observations of diurnal temperature variations on Enceladus suggest a thermal inertia that is 100 times smaller than that of water ice, implying a highly unconsolidated surface (Spencer et al., 2006). For fixed density and specific heat, this implies a conductivity 10^4 times smaller than solid ice. Thus, a model that included a 10-cm surface insulating layer with a thermal conductivity 10^4 times smaller than that of solid ice was constructed. This model yielded surface temperatures that were lower and dropped off more slowly with distance from the fracture than the uninsulated model, producing spectra that are a poor match for the CIRS data (Fig. 6). Our model therefore suggests high surface thermal inertias near the tiger stripes. This is consistent with the blue color of the surface near the tiger stripes in the Cassini ISS images (Porco et al., 2006), and strong H_2O absorptions at 1.04, 1.25, 1.5, 1.65 and 2 μm in VIMS pixels that include the tiger stripes (Brown et al., 2006; Stephan et al., 2007; Jaumann et al., 2008). Both of these observations suggest coarse-grained crystalline ice near the tiger stripes, perhaps due to sintering of surface grains by vapor condensed from the plumes, and such a process would also increase thermal inertia.
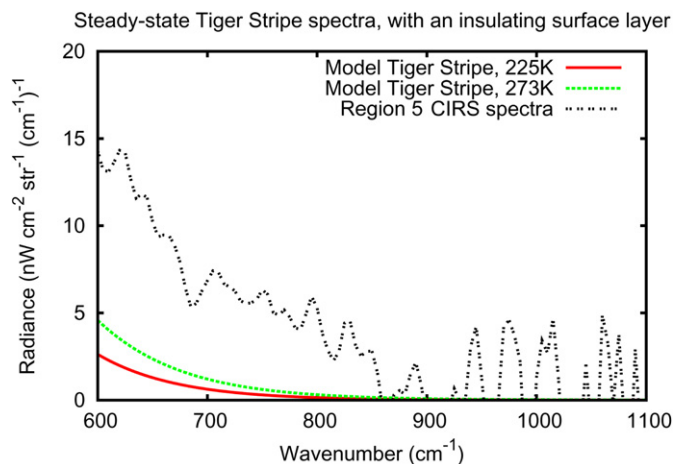
Fig. 6. Comparison of models with a 10-cm insulating (thermal conductivity 10^4 times smaller than that of pure ice) upper layer to the region 5 CIRS data. Models with a fracture temperature of 225 and 273 K are shown. Model fracture width is 0 m.

Fig. 7. Transient heating model compared to region 5 CIRS spectra. Best fit is obtained at 0.3 years. The model was started with a fracture width of 0 m and fracture temperature of 273 K and allowed to cool from equilibrium.

4.3. Transient model

Given the stability of the thermal emission seen by Cassini over 18 months, we also investigated whether this stability required constant heat input or might instead be due to long thermal time constants. A transient heating model was constructed, starting with the steady-state temperature distribution near a 273 K fracture (Fig. 2), then turning off the heat and allowing the model to cool. Even with this high initial fracture temperature, the model spectrum fell below the flux levels of the CIRS spectrum of region 5 only 0.3 years after the heat was shut off (Fig. 7). The surface cools below the detectability limit of the CIRS instrument in ∼10^3 years. These results strongly suggest that the observed CIRS spectra require constant heat input, which is consistent with the persistence of the visible plumes over several years of Cassini images (Spitale and Porco, 2007).
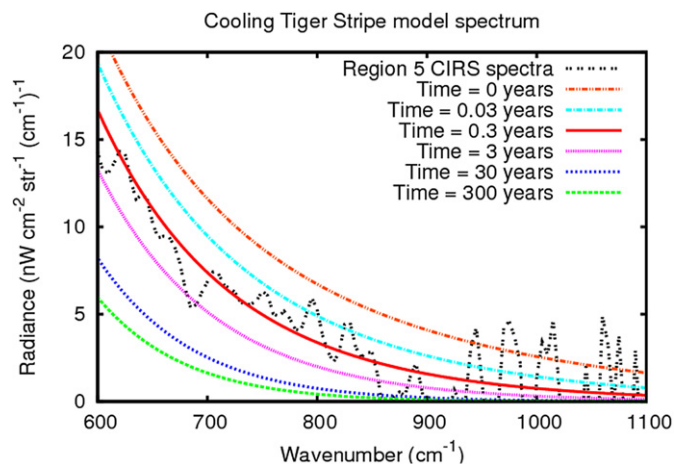
4.4. Effects of non-zero fracture width

The baseline model was further refined by introducing fracture width as a second free parameter, in addition to fracture temperature. In this model, the variable-width fracture is held at some constant temperature, and the nearby surface is heated conductively as in the baseline model. The integrated spectrum includes both the fracture (a single-temperature blackbody) and the radiation from the conductively-heated surface. The baseline model was run for fracture temperatures between 85 and 220 at 5 K increments. The best-fit fracture widths to the Region 5 and 6 CIRS spectra, and associated residuals, are shown in Fig. 8. Generally speaking, increasing the fracture temperature decreases the fracture width at which the best fit to the CIRS spectrum is obtained. The mean square residual is lowest for a fracture width of 180 m and fracture temperature of 130 K for region 5 and fracture
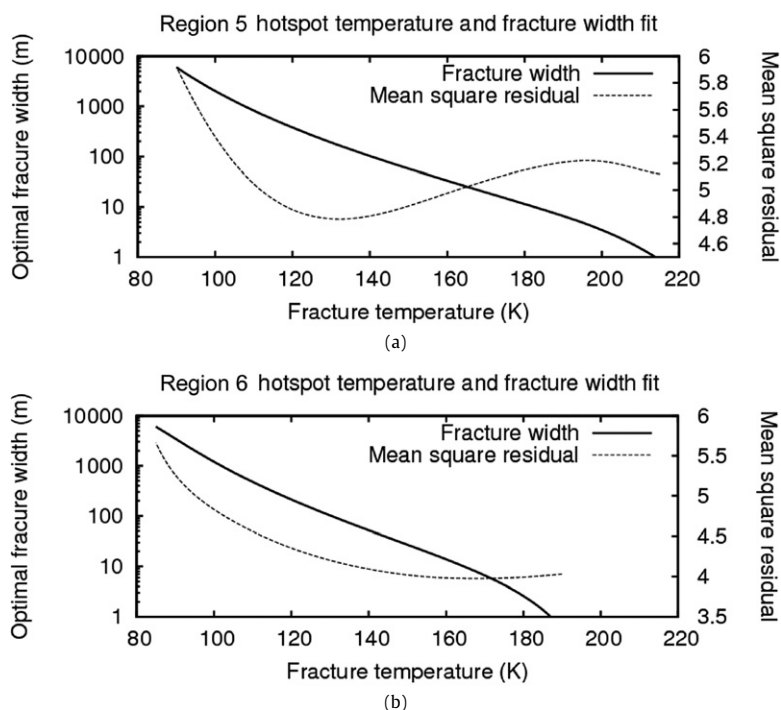

(a)

(b)

Fig. 8. Model fracture widths that produce the best fits to CIRS data for each temperature. The mean square residuals between the model and CIRS spectra are indicated by dashed lines. (a) Region 5. The minimum mean square residual occurs at a fracture width of 180 m and a temperature of 130 K. (b) Region 6. The minimum mean square residual occurs at a fracture width of 22 m and a temperature of 155 K.

width of 22 m and fracture temperature of 155 K for region 6. The fits to the CIRS data for these parameters are shown in Figs. 5c and 5d. While the spectral fits are good, four 130 km long fractures at these temperatures would supply only 0.003 and 0.5 kg/s, respectively, of water vapor to the plume if the plume is in vapor pressure equilibrium with the fracture walls and escapes at thermal speeds. This is far below the observed production rate, so on this model the fractures producing the observed thermal emission would have to be different from the fractures producing the plumes, despite the observed spatial correlation between thermal emission and plume production (Spitale and Porco, 2007).

4.5. Effects of fracture orientation and location within the footprint

The orientation of the fracture within the CIRS footprint can affect the spectrum and therefore the model fracture temperature that best matches the data. Although a tiger stripe is visible in region 5 at angle of ∼15° from the vertical side of the footprint, no obvious sources of emission are visible in the region 6 footprint. For consistency, the fractures in this work were modeled traversing the square CIRS footprint in the direction that minimizes the area of the fracture within the footprint, i.e., at an angle of 0° or 90° to the vertical. In the extreme case of a fracture traversing the CIRS footprint the longest possible way, i.e. at an angle of 45° to the vertical, model fracture temperatures that best match the data would be lower by ∼18%. Thus, temperatures presented in the paper represent the upper limit, intended to show what is possible under the described model conditions.

The location of the fracture within the CIRS footprint is of lesser importance, as the bulk of thermal emission comes from a narrow hot zone within 100 m of the fracture (Fig. 3), much smaller than the CIRS field of view.

4.6. Convecting ice thermal model

A different approach to modeling the temperature distribution in the vicinity of tiger stripes was taken by Barr and McKinnon (2007). Their model assumed convection in Enceladus' icy shell, and consequent delivery of warm material to the near-surface, as the primary heating mechanism of the tiger stripes. In essence, tiger stripes were modeled as roughly analogous to the spreading centers at terrestrial mid-ocean ridges. The vicinity of the tiger stripes is heated conductively from the central upwelling as well as from below. The temperature of the central upwelling in this model is ∼140 K, which is significantly lower than the 223 K best-fit temperature of our zero-fracture-width model. The overall temperatures in this model, shown in Fig. 9a, are significantly lower and more spread out than in the models presented in this work (e.g., Fig. 3). The resulting spectrum (Fig. 9b) is relatively close in radiance to the CIRS data from region 5. However, as Fig. 9b illustrates, it is very similar to spectra obtained from a constant-temperature surface, and is a relatively poor match to the shape of the CIRS curve.

5. Discussion

The results presented in this work constrain the heating mechanism at the tiger stripes in several ways. Transient models yield poor fits to the CIRS data, which, coupled with the short cooling timescales and a lack of detectable change in thermal output during two Enceladus flybys 16 months apart, strongly suggest that the average heat input to the active region is relatively constant over this period, though local temporal variability is certainly possible. Poor fits of the spectra from the temperature distribution generated by the convecting ice model (Section 4.6) to the CIRS data suggest that heat delivery to the surface by convecting ice is not the dominant heating mechanism of the tiger stripes. More
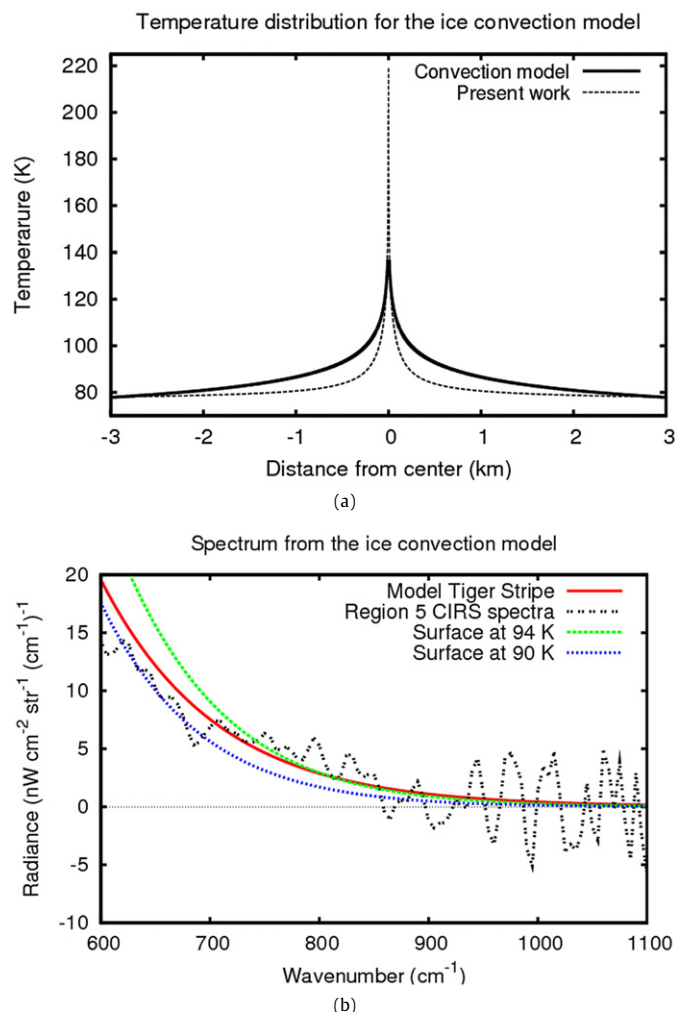

Fig. 9. (a) Temperature distribution from the ice convection model by Barr and McKinnon (2007), compared to the temperature distribution of the model with a fracture temperature of 223 K presented in this work. (b) A comparison of the spectrum from the ice convection model to region 5 CIRS data and constant-temperature blackbody spectra.

generally, the fact that the CIRS spectrum shapes require a small fraction of the CIRS field of view at high temperature rather than a general elevation of surface temperature over the whole field of view (e.g., the blackbody curves in Fig. 9) appears to rule out conductive heating from a shallow subsurface reservoir of liquid water underlying a large fraction of a CIRS field of view as the dominant heat source. A subsurface liquid water reservoir 350 m beneath the surface would result in a constant surface temperature of 90 K assuming solid-ice thermal conductivity, which results in the best blackbody fit to the region 5 CIRS data (e.g., Fig. 9b), but still a very poor fit overall. This suggests that if a subsurface reservoir exists, it is likely more than 1 km beneath the surface or is masked by an insulating surface layer. At that depth, it would result in a surface temperature of only 78 K, and would not be thermally dominant. Another scenario that is ruled out in this work is a fracture filled with liquid water near the surface, and thus having a temperature of ∼273 K. The radiance generated by conductive heating of the surface surrounding such a fracture, even if the fracture itself is close to zero width, would be significantly higher than that observed by CIRS in the regions examined (Fig. 4), unless a thin surface insulating layer is present.

The best fits to the CIRS data require localized regions at high temperatures, and are well matched with a simple model in which

a narrow warm fracture conductively heats the surrounding surface. Fracture temperatures of about 223 K are required for region 5, centered on Cairo Sulcus, if flux from the fracture itself is negligible (Fig. 5a), as is consistent with the few-cm fracture widths at these temperatures inferred from plume supply rates. Adding thermal emission from a variable width fracture into the model marginally improves the fits to the CIRS data (Figs. 5c, 5d, and 8) and allows temperatures as low as 130 K. Though these fits are as good as, or slightly better than, those with negligible fracture width (Figs. 5a and 5b), we prefer the models with negligible fracture width because they can fit the data with a single free parameter, rather than two; because the lack of emission angle dependence to the emission, discussed above, somewhat favors models where the fractures do not dominate the thermal emission; and because such wide, cool, fractures cannot supply the observed plumes. However, fine discrimination between models is not possible given the level of noise in the CIRS data.

It is important to note, however, that the 2-D modeling presented in this paper represents just one possible temperature distribution scenario. For example, it is entirely possible that thermal emission along tiger stripes is non-uniform, even within the relatively small 6-km CIRS footprint. It is certainly non-uniform on a regional scale, as shown in Fig. 1. Thus, there may be small segments along the fractures in which temperatures are significantly higher than those required by the models presented in this paper. To assess the plausibility of this scenario, 3-D modeling is required to generate temperature distributions and compare their spectrum to that of CIRS. This is outside the scope of this paper, but is a promising direction for future work. Additional observations obtained during the March 2008 flyby of Enceladus by Cassini will further constrain the temperatures and widths of the vents.

6. Conclusions

The hottest temperatures detected by CIRS in the south polar regions of Enceladus are consistent with conductive heating of the surface from a model linear fracture with a temperature as high as 223 K and negligible fracture width. Equally good fits can be obtained if emission is dominated by the fracture itself, for fracture temperatures of 130 K (region 5) and 155 K (region 6), with corresponding fracture widths of 180 and 22 m, though this scenario is less probable due to the lack of emission angle dependence of the spectra from the July 2005 and November 2006 flybys, and because vents with these temperatures and widths cannot supply the observed H_2O vapor flux. Thus, the results favor high-temperature models, namely venting from a subsurface liquid water reservoir (Porco et al., 2006; Schmidt et al., 2008), although lower temperatures predicted by clathrate decompression (Kieffer et al., 2006) and shear heating (Nimmo et al., 2007) models cannot be ruled out. The models that best match the CIRS data are characterized by small fractions of the surface at high temperatures, which strengthens the case for heat being transported to the surface along fractures rather than by conduction from a subsurface heat source or convection of overlying ice. Thus, a subsurface liquid water reservoir, if one exists, is likely more than 1 km beneath the surface. Also, a fracture filled with liquid water near the surface would produce significantly higher radiances than were detected in the study regions, and is thus inconsistent with the data, unless an insulating layer is present. Models with a 10 cm upper insulating layer produce a poor match to the CIRS spectra (unless most of the emission is from the fracture itself), indicating high thermal inertias within a few hundred meters of the tiger stripes and confirming coarse-grained crystalline ice composition derived from the ISS and VIMS data.

The relatively high temperature, coupled with a short cooling timescale of the tiger stripes, relatively constant fluxes seen by CIRS over 16 months, and poor fits to the CIRS data generated by the transient cooling model, suggests that the heat input is relatively constant over the 16 months covered by the CIRS data presented here.

References

Barr, A.C., McKinnon, W.B., 2007. Can convection start in Enceladus' ice shell? Geophys. Res. Lett. 34, doi:10.1029/2006GL028799. L09202.

Brown, R.H., Clark, R.N., Buratti, B.J., Cruikshank, D.P., Barnes, J.W., Mastrapa, R.M.E., Bauer, J., Newman, S., Momary, T., Baines, K.H., Bellucci, G., Capaccioni, F., Cerroni, P., Combes, M., Coradini, A., Drossart, P., Formisano, V., Jaumann, R., Langevin, Y., Matson, D.L., McCord, T.B., Nelson, R.M., Nicholson, P.D., Sicardy, B., Sotin, C., 2006. Composition and physical properties of Enceladus' surface. Science 311, 1425–1428.

Bryson, C.E., Cazcarra, V., Levenson, L.L., 1974. Sublimation rates and vapor pressures of H_2O, CO_2, N_2O, and Xe. J. Chem. Eng. 19, 107–110.

Childs, K.W., 1993. HEATING 7.2 User's Manual, ORNL/TM-12262, Oak Ridge National Laboratory.

Flasar, F.M., and 42 colleagues, 2004. Exploring the Saturn system in the thermal infrared: The composite infrared spectrometer. Space Sci. Rev. 115, 168–297.

Hansen, C.J., Esposito, L., Stewart, A.I.F., Colwell, J., Hendrix, A., Pryor, W., Shemansky, D., West, R., 2006. Enceladus' water vapor plume. Science 311, 1422–1425.

Jaumann, R., and 18 colleagues, 2008. Distribution of icy particles across Enceladus' surface as derived from Cassini–VIMS measurements. Icarus 193, 407–419.

Kieffer, S.W., Lu, X., Bethke, C.M., Spencer, J.R., Marshak, S., Navrotsky, A., 2006. A clathrate reservoir hypothesis for Enceladus' south polar plume. Science 314, 1764–1766.

Nimmo, F., Spencer, J.R., Pappalardo, R.T., Mullen, M.E., 2007. Shear heating as the origin of the plumes and heat flux on Enceladus. Nature 447, 289–291.

Schmidt, J., Brilliantov, N., Spahn, F., Kempf, S., 2008. Slow dust in Enceladus' plume from condensation and wall collisions in tiger stripe fractures. Nature 451, 685–688.

Porco, C.C., Helfenstein, P., Thomas, P.C., Ingersoll, A.P., Wisdom, J., West, R., Neukum, G., Denk, T., Wagner, R., Roatsch, T., Kieffer, S., Turtle, E., McEwen, A., Johnson, T.V., Rathbun, J., Veverka, J., Wilson, D., Perry, J., Spitale, J., Brahic, A., Burns, J.A., Del Genio, A.D., Dones, L., Murray, C.D., Squyres, S., 2006. Cassini observes the active south pole of Enceladus. Science 311, 1393–1401.

Spahn, F., Schmidt, J., Albers, N., Horning, M., Makuch, M., Seiss, M., Kempf, S., Srama, R., Dikarev, V., Helfert, S., Moragas-Klostermeyer, G., Krivov, A.V., Sremcevic, M., Tuzzolino, A.J., Economou, T., Grun, E., 2006. Cassini dust measurements at Enceladus and implications for the origin of the E ring. Science 311, 1416–1418.

Spencer, J.R., Pearl, J.C., Segura, M., Flasar, F.M., Mamoutkine, A., Romani, P., Buratti, B.J., Hendrix, A.R., Spilker, L.J., Lopes, R.M.C., 2006. Cassini encounters Enceladus: Background and the discovery of a south polar hot spot. Science 311, 1401–1405.

Spitale, J.N., Porco, C.C., 2007. Association of the jets of Enceladus with the warmest regions on its south-polar fractures. Nature 449, 695–697.

Stephan, K., Jaumann, R., Hansen, G.B., Clark, R.N., Buratti, B.J., Brown, R.H., Baines, K.H., Bellucci, G., Coradini, A., Cruikshank, D.P., Griffiths, C.A., Hibbitts, C.A., McCord, T.B., Nelson, R.M., Nicholson, P.D., Sotin, C., Wagner, R., 2007. Distribution of icy particles across Enceladus' surface as derived from Cassini–VIMS measurements. Lunar Planet. Sci. XXXVIII. Abstract 747.

Tian, F., Stewart, A.I., Toon, O.B., Larsen, K.W., Esposito, L.W., 2007. Monte Carlo simulations of the water vapor plumes on Enceladus. Icarus 188, 154–161.

Waite, J.H., Combi, M.R., Wing-Huen, I., Cravens, T.E., McNutt, R.L., Kasprzak, W., Yelle, R., Luhmann, J., Niemann, H., Gell, D., Magee, B., Fletcher, G., Lunine, J., Wei-Ling, T., 2006. Cassini ion and neutral mass spectrometer: Enceladus plume composition and structure. Science 311, 1419–1422.

Wan, Z., Ng, D., Dozier, J., 1994. Spectral emissivity measurements of land-surface materials and related radiative transfer simulations. Adv. Space Res. 14 (3), 91–94.